JOURNAL OF GEOPHYSICAL RESEARCH, VOL. 99, NO. D4, PAGES 8335–8350, APRIL 20, 1994

Estimation of surface albedo from space: A parameterization for global application

Zhanqing Li
Canada Centre for Remote Sensing, Ottawa, Ontario, Canada

Louis Garand
Atmospheric Environment Service, Dorval, Quebec, Canada

Abstract. This study proposes a simple parameterization to derive surface broadband albedo from satellite observations, using the results of detailed radiative transfer computations for a variety of atmospheric and surface conditions. The end result is a single equation that directly yields surface albedo from observed albedo at the top of the atmosphere, solar zenith angle, and total precipitable water. It was demonstrated that the parameterization is valid for retrieval of both instantaneous and daily mean surface albedo. Sensitivity tests were conducted for precipitable water, aerosol, CO_2, O_3, and temperature profile. Preliminary validation using collocated satellite and tower measurements indicates that the absolute accuracy requirement of 5% for climate studies is well satisfied. A global monthly climatology (excluding polar areas) of surface albedo is then developed from 5 years of Earth Radiation Budget Experiment clear-sky satellite data and European Centre for Medium-Range Weather Forecasts humidity analysis data. Examination of month-to-month differences for specific 2.5° × 2.5° areas indicate that the absolute random error on monthly estimates is less than 1%. Seasonal variation of surface albedo exceeding 1% can thus be detected. Comparisons with other satellite estimates show much closer agreement than with the values used in some general circulation models and numerical weather prediction models especially over snow/ice and deserts.

1. Introduction

Surface albedo is an important parameter influencing the Earth's climate, since it directly affects the solar energy absorbed by the surface, which in turn modifies, through feedback processes, the various components of the climate system. Of consequence, the Earth's climate is very sensitive to changes in surface albedo caused by both natural variations and human activities [*Charney et al.*, 1977; *Potter et al.*, 1981, 1983]. It was demonstrated that ice-albedo and biosphere-albedo feedbacks are critical to climate modeling [*Lian and Cess*, 1977; *Cess*, 1978]. *Henderson-Sellers and Wilson* [1983] recommended that a global surface albedo data set be developed within the next 5–10 years for climate studies with an absolute accuracy of 5% for a spatial scale of 1°–2° latitude and longitude and timescale of 7–10 days. Ten years later, we still cannot claim that this seemingly modest goal has been achieved. *Barker and Davies* [1989], for example, found that among six general circulation models (GCMs), surface albedo values differ by more than 10% for the Earth's major deserts. Furthermore, for less reflective surfaces, a relative accuracy of 15% may be desirable. Because of its effect on surface temperature, surface albedo is also used in short-range numerical weather prediction (NWP). In addition to the significance for meteorological studies, observation of surface albedo provides a means of monitoring environmental changes associated with human activities such as harvesting, deforestation, and desertification.

Although surface albedo has been routinely observed for a long time, a global climatology of surface albedo can hardly be developed from such measurements. This is because ground-based observations can only represent a very small area, and surface albedo often varies greatly at small spatial scales [*Ohmura and Gilgen*, 1993]. Traditionally, global data sets of surface albedo were obtained by classification of the Earth's surface types and assigning typical albedo values to these surface types. The first data set of this kind was acquired by *Posey and Clapp* [1964] and was used in several GCMs during the 1970s [*Henderson-Sellers and Wilson*, 1983]. A comprehensive global archive of surface types was made by *Wilson and Henderson-Sellers* [1985]. In their compilation, global soil type and land cover data were extensively explored at a resolution of 1° × 1°. This data set, however, suffers from the lack of information on seasonal variability. The seasonal cycle of zonally averaged surface albedo was derived for 10° latitude bands by *Robock* [1980] and for 2° bands by *Kukla and Robinson* [1980], using land classification data and satellite-estimated snow cover data. Monthly mean albedos at the surface and at the top of the atmosphere (TOA) were computed on 5° × 5° and 1° × 1° grids by *Briegleb and Ramanathan* [1982] and *Briegleb et al.* [1986], respectively.

Satellite observations constitute the only available means for global repetitive monitoring of the surface. They allow the establishment of a global climatology of albedo at homogeneous resolution with less arbitrariness and minimal effort.

Published in 1994 by the American Geophysical Union.

Paper number 94JD00225.

The principle permitting the estimation of surface albedo from space is that the observed albedo at the top of the atmosphere (hereafter referred to as TOA albedo) is mainly controlled by surface albedo under clear skies. Major challenges include clear scene identification, spectral and angular corrections and the removal of atmospheric effects [*Sellers et al.*, 1990; *Choudhury*, 1991]. Identification of clear skies is the first step in the process. Since clouds cover more than half the globe at any particular time, compositing of clear pixels is necessary over a certain period. Some studies [*Preuss and Geleyn*, 1980; *Pinty and Szejwach*, 1985] assumed that the minimum value of albedo measured represents clear-sky albedo, but this simplistic assumption generally leads to underestimation of surface albedo [*Matthews and Rossow*, 1987; *Gutman*, 1988].

Depending on the nature of the study, both spectrally dependent and broadband albedo may be needed. For example, many GCMs require surface albedo for at least two spectral intervals: visible and near-infrared [*Dickinson*, 1983], whereas radiation budget studies need broadband values to separate downwelling and net solar irradiance. If one is interested in broadband albedo, an uncertainty may arise from the use of narrowband measurements made by operational satellites such as METEOSAT [*Preuss and Geleyn*, 1980; *Pinty and Szejwach*, 1985; *Pinty and Ramond*, 1987], GMS [*Nunez et al.*, 1987], NOAA [*Matthews and Rossow*, 1987; *Gutman et al.*, 1988, 1989a] or LANDSAT [*Brest and Goward*, 1987]. Comparison of simultaneous and collocated narrowband advanced very high resolution radiometer (AVHRR) reflectance and broadband Earth Radiation Budget Experiment (ERBE) reflectance reveals significant differences [*Li and Leighton*, 1992]. The use of broadband measurements removes this potential problem. Besides, broadband sensors such as ERBE or NIMBUS-7 are much better calibrated than narrowband sensors due to the lack of inflight calibration for operational satellites. For example, calibration accuracies for shortwave radiance of METEOSAT and ERBE are about 10% [*Arino et al.*, 1991] and 2–3% [*Barkstrom et al.*, 1989], respectively. In principle, one may derive spectral albedo from broadband albedo using some standard spectral functions that are dependent on surface type.

Another related issue concerns the correction of angular variations in albedo, which include bidirectional and directional dependencies. A bidirectional function is used to convert a reflectance measurement made in a specific direction into an albedo defined over all directions for a given solar zenith angle (SZA). Bidirectional correction is one of the most sensitive factors in the inference of surface albedo from satellite measurements [*Koepke and Kriebel*, 1987]. Unfortunately, most previous attempts failed to account for the bidirectional effect owing to the shortage of bidirectional models and the difficulty in determining the parameters of a bidirectional model. *Gutman et al.* [1989b] applied the ERBE broadband bidirectional models to AVHRR data to derive TOA albedo. After bidirectional correction, the albedo still depends on solar zenith angle. Directional models account for this dependency to infer either the daily mean albedo or the normalized albedo at any specific SZA from the derived albedo at a given SZA.

In view of the problems mentioned above, the ERBE satellite program has some unique advantages [*Barkstrom and Smith*, 1986]. It has a scene identification algorithm, in-flight calibration of broadband observations and bidirectional and directional corrections, although none of these procedures are free of errors. In addition, ERBE allows good spatial and temporal sampling at medium resolution. ERBE includes three spacecrafts: two NOAA satellites flying in polar orbits and one Earth Radiation Budget Satellite (ERBS) in precessing orbit. The former provides measurements at about the same local times, while the latter renders observations through 24 local hours in about 36 days. The nadir footprints of the ERBE scanning radiometers are of the order of 40 km. ERBE has 12 sets of scene-dependent angular models which are applied to derive TOA albedos according to the results of the ERBE scene identification algorithm.

To derive surface albedo from TOA albedo, the influence of the intervening atmosphere has to be removed. To this end, some investigators such as *Preuss and Geleyn* [1980], *Chen and Ohring* [1984], *Pinker* [1985], and *Koepke and Kriebel* [1987] have linearly related TOA and surface albedos. Others [*Pinty and Szejwach*, 1985; *Barker and Davies*, 1989] have made use of radiation models to estimate surface albedo by equating the TOA albedo obtained from satellite observation with a model value. The simplicity of a linear relationship makes it promising for processing large amounts of satellite data, provided it can attain an acceptable accuracy. To date, the majority of such relationships were developed using results from simplified radiative transfer calculations in which either spectral or angular variations, or both, were neglected. The validity of the linear relationship was thus questioned [e.g., *Matthews and Rossow*, 1987]. Besides, most algorithms were not presented in such a way that they were readily useful for global application.

Detailed radiative transfer calculations were conducted for the present study in order to incorporate different atmospheric conditions for a variety of surface types characterized by different spectral and angular dependencies of albedo. Section 2 outlines the model and radiative transfer simulations. The outputs of the computations are used to examine the linearity of the relationship between TOA and surface albedos in section 3. This section also investigates and parameterizes the effects of different parameters on the relationship. Section 4 presents sensitivity tests and validation results using collocated satellite and tower measurements. Section 5 deals with the regional, zonal, and seasonal variations of the global monthly surface albedo at 2.5° × 2.5° resolution derived from the parameterization using 5 years of ERBE clear-sky TOA albedo data and precipitable water data from the European Centre for Medium-Range Forecasts (ECMWF) archive. A summary is presented in the last section.

2. Model and Simulations

Radiative transfer simulations are carried out with a double-adding model applied to a plane-parallel vertically inhomogeneous system [*Masuda and Takashima*, 1986, 1988; *Li et al.*, 1993a]. The extraterrestrial solar spectrum data compiled by *Iqbal* [1983] are adopted. The solar spectrum from 0.285 to 5.0 μm is divided into 108 wavelengths consisting of 83 unequal intervals from 0.285 to 2.5 μm and 25 equal intervals of 0.1 μm beyond 2.5 μm. The optical thickness that is due to molecular absorption is obtained from transmittances computed by LOWTRAN 6 [*Kneizys et*

al., 1983]. The optical properties of aerosol are calculated from Mie theory. An ozone amount of 350 Dobson units is used. The subarctic summer model atmosphere [*McClatchey et al.*, 1971] and the aerosol model 3 of *Blanchet and List* [1983] are employed in the simulations. There are no specific reasons for choosing such a type of atmosphere but the original objective of the work [*Li et al.*, 1993a]. Sensitivity tests (section 4) show that the temperature profile and most of the atmospheric constituents such as CO_2 and O_3 have negligible effects on the relationship between TOA albedo and surface albedo. However, some effects of water vapor are noted. Therefore various water vapor loadings are considered by scaling the subarctic summer model water vapor profile. For each atmospheric and surface condition, calculations were made for 15 solar zenith angles ranging from 0° to 90°. Aerosol effects will be discussed further.

Four typical surface types are selected, namely, ocean, vegetated land, desert, and ice/snow. The ocean is assumed to be a semi-infinite water body with wind speed of 5 m/s. Its scattering and absorption coefficients are defined by *Masuda and Takashima* [1986]. Ice/snow spectral albedo is computed using the double-adding code for ice crystal properties obtained following the approach of *Wiscombe and Warren* [1980]. Mean grain sizes of 50, 200, 1000, and 2000 μm are assumed to represent fresh, old, near melting, and melting snow/ice conditions, respectively. The thickness of snow/ice is 2 m. To allow for anthropogenic contamination, trace amounts of graphitic soot with a mass fraction of 0.05 ppmw are included [*Warren and Wiscombe*, 1980; *Tsay et al.*, 1989]. The large variety of land surfaces may be spanned by choosing areas of bog and desert for the study. The former represents dense vegetated land and the latter bare land.

Figure 1 illustrates the spectral dependency of surface albedo at a SZA of 60° for ocean, vegetated land, desert, and snow/ice of grain sizes decreasing from 2000 μm to 50 μm.

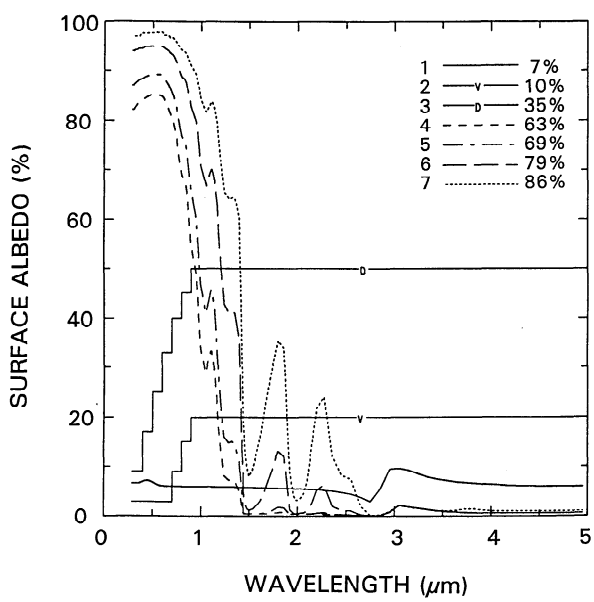

Figure 1. Dependence of spectral surface albedo on wavelength at SZA = 60° for ocean (1), vegetated land (2), desert (3), and snow/ice of various ages: melting (4), nearly melting (5), old (6) and fresh (7). Albedos for land and desert were taken from *Cess and Vulis* [1989]. The values of broadband albedo are included. [after *Li et al.*, 1993a].

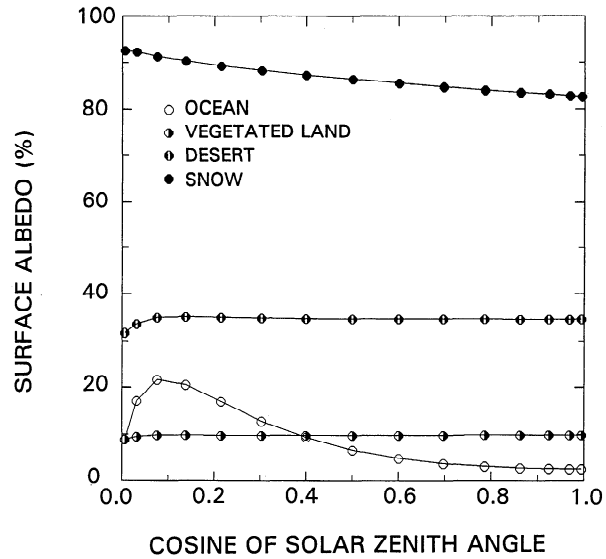

Figure 2. Dependence of surface albedo on SZA for ocean, vegetated land, desert, and fresh snow/ice.

The corresponding broadband surface albedos are 7%, 10%, 35%, 63%, 69%, 79%, and 86%. Spectral variations of the albedo are simulated by the model for all types of surface except land, whose spectral reflectance is controlled by many factors such as soil type, moisture, vegetation density, and type, etc. Modeling these effects is beyond the scope of the study. Simplified spectral functions of the atmosphere-free albedo for bog and desert shown in Figure 1 are taken from *Cess and Vulis* [1989]. They are based on the measurements made by *Kriebel* [1978] for bog and *Whitlock et al.* [1987] for the Sonora Desert in Arizona. They are the two extreme categories of land considered by *Cess and Vulis* [1989] to span the diversity of land surfaces. As a result, the simplified functions may differ considerably from specific observations of the spectral dependency made by *Bowker et al.* [1985] over a variety of land types.

Figures 2 and 3 show the surface and TOA albedos as functions of the cosine of the SZA simulated from radiative transfer calculations. Note that the surface albedos of ocean and snow are subject to the strongest changes with varying SZA. The drop of ocean surface albedo at large SZA is due to the effects of oceanic waves resulting from a wind speed of 5 m/s over the ocean surface employed in the simulation. The wave effects were demonstrated by *Cox and Munk* [1956]. The weak dependency of surface albedo on the SZA for vegetated land and desert is attributed to the effects of the atmosphere, since atmosphere-free land surfaces are assumed to be Lambertian. Comparison of Figures 2 and 3 indicates that the angular dependence of TOA albedo is quite different from that of the surface due to the presence of the atmosphere.

The negligence of the angular dependency for land surfaces is partially due to the paucity of the observations for spectral-dependent angular models throughout the solar spectrum. Bidirectional measurements made by *Kriebel* [1978] and *Whitlock et al.* [1987] are restricted to wavelengths between 0.20 and 2.2 μm. The negligence is also due to the difficulties associated with the simulation of angular dependence models outlined by *Pinty and Verstraete* [1992]

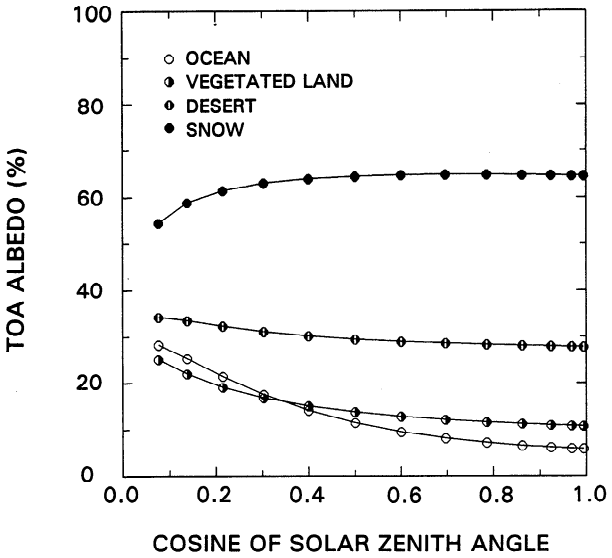

Figure 3. Same as Figure 2 but for TOA albedo obtained from radiative transfer simulations with precipitable water content 1.6 cm and an aerosol optical depth of 0.05.

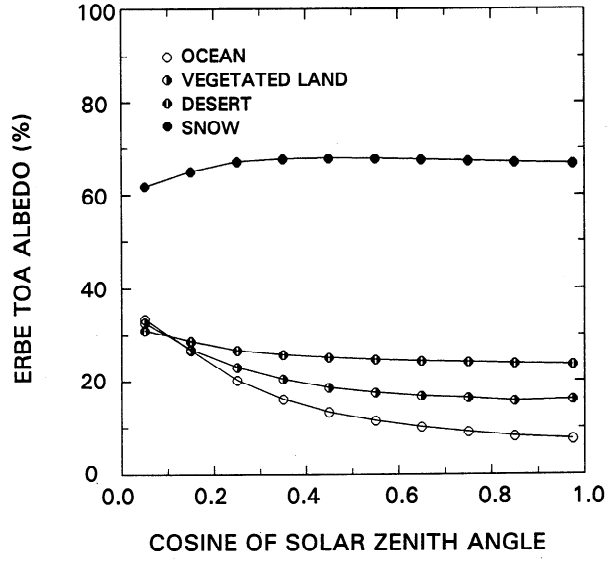

Figure 4. Dependence of TOA albedo on SZA employed by the ERBE. [after *Suttles et al.*, 1988].

and due to the dependence of the angular model on a spatial scale. Although many investigators [*Kimes*, 1983, 1984; *Sellers*, 1985; *Dickinson et al.*, 1987; *Verstraete*, 1988; *Verstraete et al.*, 1990] have developed complex models to study the anisotropic properties of terrestrial surfaces, most rely on numerous assumptions about the canopy. They include vertically semi-infinitive, horizontally and optically homogeneous, and random distribution of leave orientation. Many of the assumptions hold for a small homogeneous area which may explain the good comparison with observations made by radiometers of fine resolution [*Kimes et al.*, 1987; *Pinty et al.*, 1990; *Dickinson et al.*, 1990]. Since the anisotropy of a surface is scale-dependent, the anisotropy of a large area as viewed by a low-resolution sensor may be quite different from that derived for a small homogeneous surface [*Pinty and Verstraete*, 1992]. A large field of view (FOV) tends to average out the natural spatial variation of the angular dependence. *Pinker and Stowe* [1990] found that the simulations with a Lambertian surface produce similar patterns of bidirectional reflectance at the TOA to those obtained from NIMBUS 7 satellite observations made over land surfaces. This may suggest that the TOA bidirectional properties of the land reflectance is mainly controlled by the atmosphere for a spatial resolution like NIMBUS 7. The ERBE angular models were derived mainly from the observations made with NIMBUS 7 [*Suttles et al.*, 1988]. A limited number of GOES data and model simulation data were employed to fill the angular bins where no or few measurements exist. Figure 4 shows the angular dependence of TOA albedo used by the ERBE. Comparison of Figures 3 and 4 shows that the angular variations of TOA albedo with the SZA obtained from current simulations with the Lambertian assumption are very similar to those used by the ERBE. Some difference in terms of absolute value of albedo is expected for vegetated land, as the ERBE angular models were derived from the measurements made over a variety of land types.

The above discussion indicates that the variety of the albedos considered here represents the diversity of natural surface types and that the radiative transfer model is able to characterize the spectral and angular dependencies for these surface types.

3. Relationship Between TOA and Surface Albedos

3.1. Reexamination of the Linear Relationship

Figure 5 presents the relationship between the TOA and surface albedos for 240 simulations that combine eight surface types and six water vapor loadings. They include ocean with precipitable water 0.5, 1.1, 1.6, 2.1, 3.1, and 5.1 cm; vegetated land and desert with precipitable water 1.6 and 3.1 cm; fresh snow with precipitable water 0.5, 1.1, 1.6, and 2.1 cm and three types of aging snow with precipitable

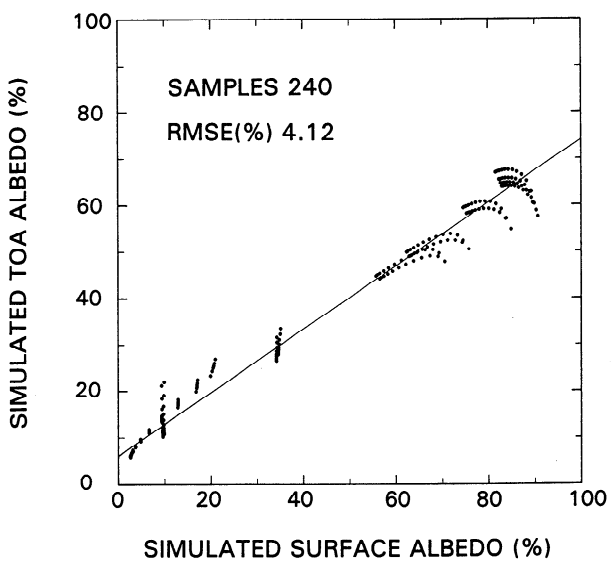

Figure 5. Comparison of TOA and surface albedos simulated for partial combinations of seven surface types, six water vapor loadings, and 13 SZAs. The straight line is a linear fit to the simulated data.

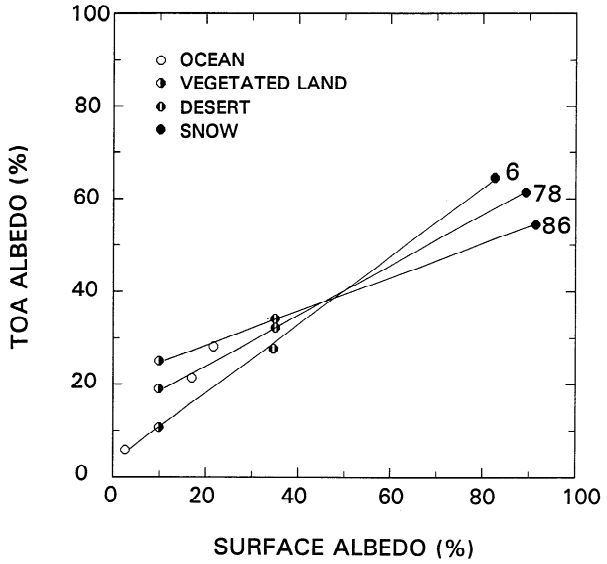

Figure 6. The relationship between TOA and surface albedos for four typical surface types at three fixed SZAs as indicated by the numbers (in degrees) on the plot. Straight lines are regression fits to the simulations.

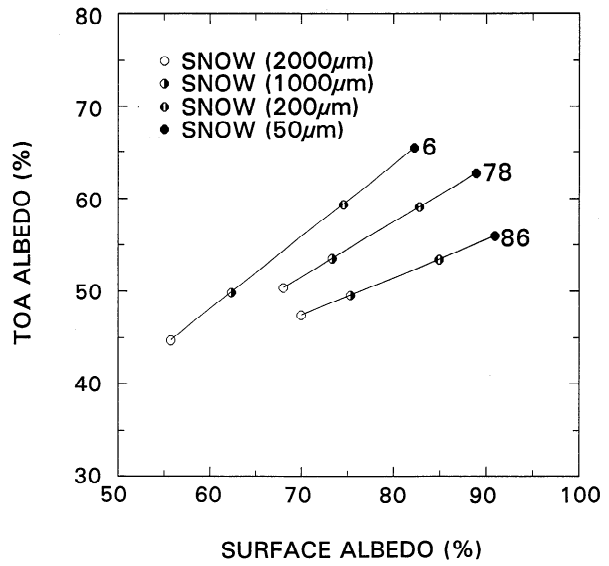

Figure 7. Same as Figure 6 but for snow/ice surfaces only.

water 1.1 and 2.1 cm. Selection of these combinations arises from both physical considerations and artificial extension of the diversity. The results for the three largest SZAs are excluded in Figure 5, since the radiative transfer calculation is less reliable at large SZA. It follows from Figure 5 that the surface albedo is grossly correlated with TOA albedo in a linear manner. On the basis of the simulated data, a linear regression can be developed to estimate surface albedo from TOA albedo, as shown by the straight line in the plot. Use of such a single regression model results in a root-mean-square error (rmse) of 4.12% in the estimate of surface albedo. *Chen and Ohring* [1984] obtained a rather small rmse of 2.8% using their single regression model, presumably due to the limited conditions that were simulated and the use of a simplified radiative transfer algorithm and surface reflectance models. Considering the uncertainties existing in other steps of the procedure such as clear scene identification, bidirectional correction, and satellite calibration, the real accuracy of the estimates of surface albedo from satellite measurements may not satisfy the requirement for climate studies if a single linear relationship is employed.

As noted by *Chen and Ohring* [1984], and *Koepke and Kriebel* [1987], the SZA accounts for a large fraction of the variability in the relationship. The variability due to SZA is indicated by the spread of a series of points falling along one curve in the clusters shown in Figure 5 which have the same atmospheric and surface conditions but varying SZA. Indeed, if the TOA and surface albedos are related at fixed SZA, the relationship becomes much more linear, as shown in Figure 6. The nonlinearity appears very weak, as indicated by the deviations of the points from the linear regression lines. The weak nonlinearity arises basically from the difference in the dependence of surface albedo on wavelength and SZA for different surface types. This conclusion is inferred from the finding that the relationship becomes purely linear if the same surface type is selected such as snow/ice of different ages, whose albedos have similar spectral and angular dependencies but different magnitudes (Figure 7). It also follows from Figures 6 and 7 that the linear relationship is strongly dependent on the SZAs, especially at large SZA. As shown in Figure 6, the difference in the relationship for SZAs of 78° and 86° is larger than that for SZAs of 6° and 78°.

In addition to the SZA, precipitable water is another factor that significantly influences the linear relationship. Figure 8 shows the same relationship at fixed SZAs for different precipitable water amounts over ocean and fresh snow surfaces. The linear relationship is more sensitive to precipitable water when the atmosphere is very dry. As precipitable water decreases, the relationship approaches 1:1 line, implying that TOA albedo is closer to surface albedo. When precipitable water is abundant, TOA albedo is significantly lower than surface albedo due to strong water vapor absorption. Furthermore, the effect of precipitable water on the

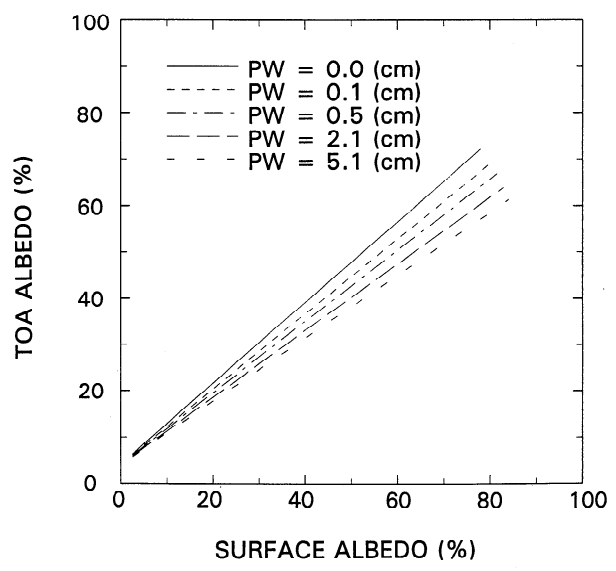

Figure 8. The relationship between TOA and surface albedos for different contents of precipitable water at SZA of 6°. The lines are obtained by using the simulation results over ocean and fresh snow surfaces.

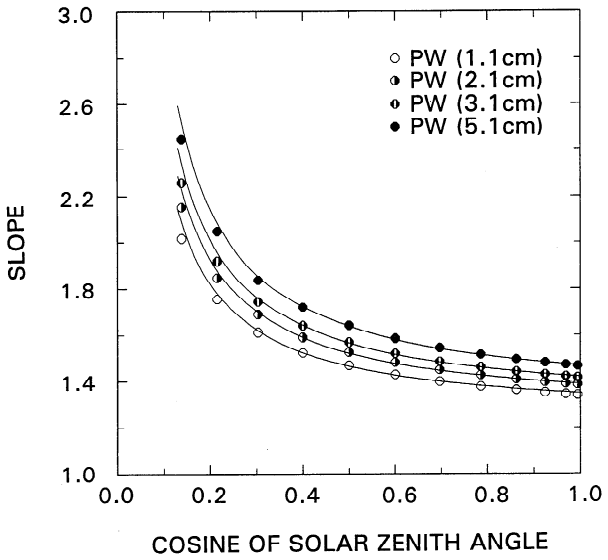

Figure 9. The variation of the slope $\beta(\mu, p)$ with the cosine of the SZA. The values shown by the points are obtained from the results of radiative transfer calculations for ocean and different ages of snow surfaces at fixed SZA and precipitable water.

relationship increases as the SZA increases (not shown here), since the influence of precipitable water on TOA and surface albedos is reinforced as the SZA increases. The physical meaning of the relationship was discussed in several previous studies such as those of *Chen and Ohring* [1984] or *Koepke and Kriebel* [1987], who expressed TOA albedo as a linear function of surface albedo. In their relationship, the intercept represents the contribution of atmospheric reflection to TOA albedo, while the slope measures the effective two-way atmospheric transmittance. Water vapor affects atmospheric reflection and transmittance via its effect on atmospheric absorption. The SZA modifies the path length of a photon in the processes of both scattering and absorbing.

3.2. Parameterization

The complicated effects of SZA and precipitable water on the linear relationship can be clearly illustrated in the plots of slope and intercept as functions of the SZA and precipitable water (Figures 9 and 10). The values of slopes and intercepts are obtained by linear regressions of the surface and TOA albedos simulated at the same SZA for different surface types. The values of slope and intercept involving the dependency on SZA are then fitted against precipitable water. The following parameterization is derived:

$$a_s = \alpha(\mu, p) + \beta(\mu, p)a_t \tag{1}$$

$$\alpha(\mu, p) = \alpha_1(p) + \alpha_2(p)\frac{1}{\mu} \tag{2}$$

$$\beta(\mu, p) = \beta_1(p) + \beta_2(p)\frac{1}{\mu} \tag{3}$$

$$\alpha_1(p) = -0.96882 + 0.71800\sqrt{p} \tag{4}$$

$$\alpha_2(p) = -4.11460 - 0.76347\sqrt{p} \tag{5}$$

$$\beta_1(p) = 1.16711 + 0.05963\sqrt{p} \tag{6}$$

$$\beta_2(p) = 0.07514 + 0.04105\sqrt{p}, \tag{7}$$

where a_s and a_t denote surface and TOA albedos, respectively; μ represents the cosine of SZA and p denotes precipitable water in centimeters. Note that the curves in Figures 9 and 10 fit very well the slopes and intercepts that are determined from the results of radiative transfer calculations. The match is limited to μ larger than 0.1. This is not only due to the fact that plane-parallel radiative transfer calculations are unreliable at very large SZA, but also to the fact that both slope and intercept change dramatically at large SZA. The procedure for the parameterization is similar to that used by *Li et al.* [1993a].

Apart from SZA and precipitable water, other atmospheric parameters such as aerosols have some effects on the relationship (section 4 of this study) [also *Koepke and Kriebel*, 1987]. However, global data on aerosol are currently difficult to obtain. The parameters of aerosol including optical depth, single-scattering albedo, phase function, and height distribution can only be roughly approximated. In this study, the optical depth of 0.05 at 0.55 μm is used, which is considered a typical aerosol loading for a clear atmosphere [*Koepke and Kriebel*, 1987; *Shaw*, 1982].

The efficiency of the parameterization is tested by substituting the simulated TOA albedos, SZAs, and precipitable water into (1)–(7) to estimate surface albedos. The estimated surface albedos are then compared with simulated surface albedos obtained from the same radiative transfer computations. Figure 11 presents the comparison of 240 pairs of surface albedos obtained from model simulations and from the parameterization. The 240 simulations are the same as those presented in Figure 5. Figure 11 shows that the parameterization can accurately reproduce the surface albedos using the three basic input parameters, the fitting error being 0.8% given by the rmse.

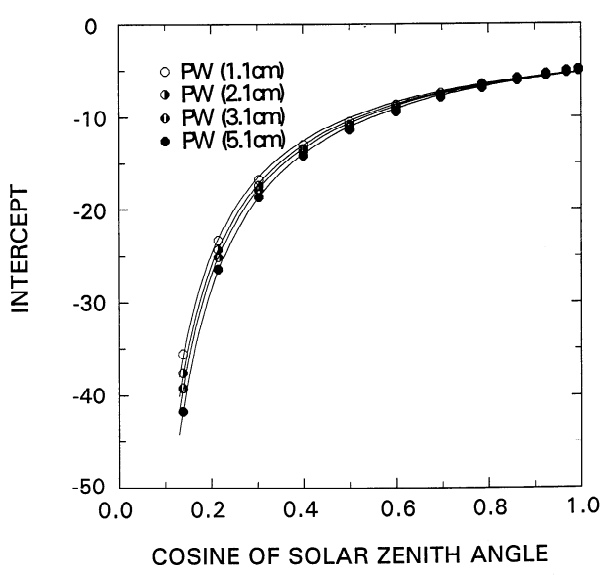

Figure 10. Same as Figure 9 but for the intercept $\alpha(\mu, p)$.

3.3. Validity for the Estimation of Daily Mean Surface Albedo

The parameterization was developed for instantaneous surface albedo retrievals. For many applications the daily mean albedo is required. Although (1) is linear with respect to a_t, it is not obvious that the daily mean surface albedo can be derived from the daily mean TOA albedo, using the same parameterization. Note that the daily mean albedo is defined as an energy-weighted quantity, not a time average of $a(t)$, that is,

$$\bar{a} = \frac{\int_{-T}^{T} I(t)a(t)\,dt}{\int_{-T}^{T} I(t)\,dt} = \frac{\int_{-T}^{T} R(t)\,dt}{\int_{-T}^{T} I(t)\,dt}, \tag{8}$$

where I and R denote incident and reflected fluxes respectively, t is local solar time, and T is the half-day length which varies according to latitude and season [*Paltridge and Platt*, 1976]. Assuming that $I(t)$ and $R(t)$ are symmetrical about midday, the integration may be calculated for a half-day. Because of the complex and diverse angular dependencies of both surface and TOA albedos, $\bar{a}$ cannot be solved analytically. We can, however, compute daily mean surface and TOA albedos using the results of the radiative transfer simulations. To do so, the integration variable is switched from t to μ, as the instantaneous values of I and R are available at specific SZAs. The cosine of the SZA is related to local time by

$$\mu = \sin\phi \sin\delta + \cos\phi \cos\delta \cos(ct), \tag{9}$$

where c is equal to $2\pi/24$hr, a conversion factor from hour angle to local solar time. Parameters ϕ and δ denote latitude and declination, respectively. From (9), the conversion function is obtained as

$$f(\mu) = \frac{dt}{d\mu} = -\frac{1}{c\sqrt{(\cos\phi\cos\delta)^2 - (\mu - \sin\phi\cos\delta)^2}}. \tag{10}$$

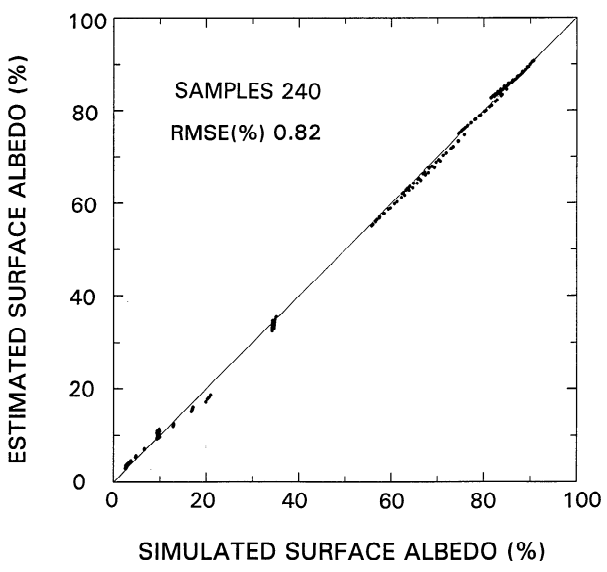

Figure 11. A comparison of the simulated surface albedos and those estimated from the parameterization using the simulated TOA albedos, SZA, and precipitable water.

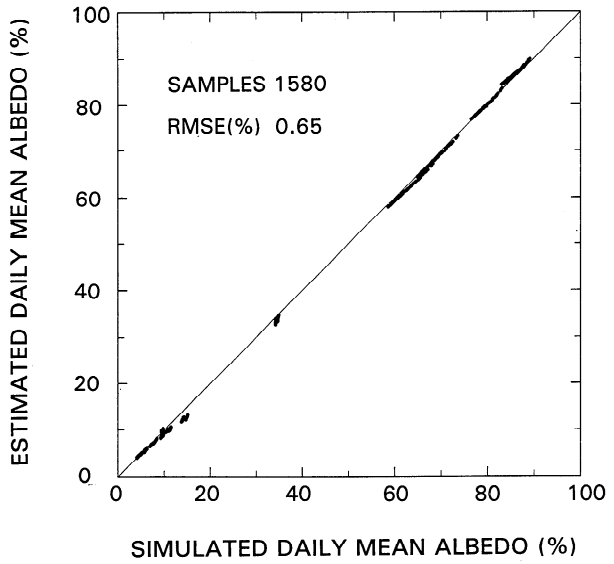

Figure 12. Same as Figure 11 but for daily mean surface albedos.

Numerical integration of (8) is thus expressed as

$$\bar{a} = \frac{\sum_{i=m}^{n} R(\mu_i) f(\mu_i) \Delta\mu_i}{\sum_{i=m}^{n} I(\mu_i) f(\mu_i) \Delta\mu_i}, \tag{11}$$

where μ_i denotes the 15 discrete values of μ. Substituting the values of $I(\mu_i)$ and $R(\mu_i)$ at surface and TOA into these equations, 1580 pairs of surface and TOA albedos are simulated for latitudes ranging from the equator to the pole over 12 months using the results of radiative transfer calculations for four different surface types. From (9), the daily mean cosine of the SZA can be computed by

$$\bar{\mu} = \frac{1}{T}\int_0^T \mu(t)\,dt = \sin\phi \sin\delta + \frac{1}{cT}\cos\phi\cos\delta\sin(cT) \tag{12}$$

The computed daily means of TOA albedo, cosine of SZA and precipitable water are then substituted into the parameterization to estimate the daily mean surface albedos. Figure 12 presents the comparison of the computed and estimated daily mean surface albedos. It is found that the agreement is as good as for instantaneous values, the rmse being 0.65%. This suggests that the parameterization is also applicable in deriving the daily mean surface albedo.

4. Sensitivity Tests and Validation

4.1. Sensitivity Tests

Sensitivity tests on the linear relationship of various factors including anisotropic conversion factor, aerosol, and precipitable water have been carried out by *Koepke and Kriebel* [1987]. In their study the test for precipitable water

was made by assuming a constant uncertainty in precipitable water. The uncertainty of precipitable water was analyzed in detail by *Li et al.* [1993a] using the climatological data. For example, the uncertainty in daily mean precipitable water δp, resulting from the use of the monthly mean precipitable water p, changes dramatically with latitude and season. This makes the error analysis using a constant δp hold only for a specific latitude and season. Li et al.'s study also showed that the relative uncertainty defined as $\delta p/p$ also varies with latitude and season. What was found to be relatively invariant is the ratio of $\delta p/\sqrt{p}$, which has a much weaker dependency on both season and latitude, with a mean value close to 0.7 (p in centimeters).

Coincidentally, the error in the estimate of surface albedo, δa_s, resulting from the uncertainty of precipitable water δp happens to be a function of $\delta p/\sqrt{p}$, which can be obtained by differentiating the parameterization with respect to precipitable water:

$$\delta a_s = 0.5\left[0.71800 - 0.76347\,\frac{1}{\mu} + \left(0.05963 + 0.04105\,\frac{1}{\mu}\right)a_t\right]\frac{\delta p}{\sqrt{p}} \qquad (13)$$

Since the value of $\delta p/\sqrt{p}$ is approximately a constant, δa_s varies basically according to SZA and TOA albedo. Except at large SZA (small μ), the uncertainty in the estimate of surface albedo due to the use of climatological data of precipitable water is not very large. When the cosine of the SZA is larger than 0.3, the uncertainty ranges from 0.2% to 1.5%, as the TOA albedo increases from 0.0% to 50%. It should be noted that precipitable water is known more precisely than climatology on the global scale from both satellite observations and model analyses [*Liu et al.*, 1992]. Operational humidity analyses provide typical errors in the order of 10% (e.g., $\delta p = 0.5$ cm for $p = 5$ cm) leading to $\delta p/\sqrt{p}$ of about 0.23. As a consequence, it is expected that errors in a_s due to errors in precipitable water will rarely exceed 1%.

Sensitivity tests to the temperature profile and other atmospheric variables including ozone, carbon dioxide, and aerosols were conducted by means of radiative transfer computations. The computed a_t was used in the parameterization along with the corresponding values of p and μ to calculate a_s. Difference in a_s resulting from different temperature profiles or concentrations of the variables provides a measure of the corresponding uncertainty in the estimate of a_s. Simulations using middle latitude summer and winter atmospheres produce a TOA albedo difference of 3.2%. To a large extent, however, the difference is attributed to the discrepancy in precipitable water content of the two model atmospheres (2.06 cm), since use of the same integrated water vapor leads to almost the same TOA and surface albedos. Uncertainty due to the concentration of CO_2 causes a negligible error since doubling it to 660 ppmv results in a calculated a_s differing by less than 0.2%. Doubling the ozone concentration results in calculated a_s values decreasing by less than 1% except when a_s is large (>80%), in which case the decrease can reach 2%.

Finally, tests were made with no aerosol and with an aerosol optical depth of 0.25 in the lowest kilometer of the atmosphere. For surface albedos of 10%, 40%, and 80%, the differences in computed a_s from the parameterization (with aerosol minus no aerosol) were 2.4%, 0.8%, and −1.3%, respectively. Thus errors due to aerosol uncertainty are highest for extreme values of surface albedo and lowest for albedos near 50%, which is close to the maximum albedo of the brightest desert such as Sahara (section 5.2). High loading and large variability in aerosol are often observed over deserts. In comparison, the atmospheres over low-reflective ocean surface or over high-reflective snow/ice surface are relatively clean. The most severe dust outbreaks over oceans should be detected as nonclear cases by the satellite scene identification algorithm.

4.2. Validation of the Estimates of Instantaneous Surface Albedo

Validation of the parameterization requires simultaneous and collocated measurements of broadband TOA and surface albedos observed from space and on the ground. To obtain data with varying μ, we used TOA albedo measurements made from the scanning radiometers aboard the ERBS, one of the three spacecrafts carrying the ERBE packages. ERBS has an orbit inclined 57° relative to the equator which allows observations at different local times with various values of μ. The nadir footprint of the ERBS scanner is roughly 35 km in diameter. Because of the large difference in the field of view of satellite and surface radiometers, routine observations at meteorological stations are not suitable for the validation of the surface albedos derived from satellite data. To better match the satellite and surface measurements, the surface albedos observed at the top of two observation towers are employed: the Boulder Atmospheric Observatory (BAO) tower at Boulder, Colorado, and another one located near Saskatoon, Canada. The same matched data sets have been employed for the validation of surface net solar irradiance estimated from ERBE observations [*Cess et al.*, 1991; *Li et al.*, 1993b] and for the assessment the impact of cloud on the shortwave radiation budget of the surface-atmosphere system [*Cess et al.*, 1993; *Nemesure et al.*, 1994].

Both towers are surrounded by plain agricultural land. The pyranometers on the BAO tower are mounted 300 m above the ground whose FOV is close to 35 km for a maximum viewing angle of 89°. This does not mean that the two types of measurements are fully comparable because the response of a radiometer is proportional to the cosine of the incident angle. The incident angle of the reflected radiance measured by a space-borne scanner with a telescope is around zero, whereas the radiance reaching the pyranometer has an incident angle ranging from 0° to 90°. In other words, the pyranometer albedo measurements are most sensitive to the radiance reflected from a region around the nadir. However, the albedo over this region may not represent the mean reflectivity over the whole FOV of a satellite pixel. To account for this, a meticulous procedure was followed to collocate two types of measurements [*Cess et al.*, 1991]. The Boulder tower data were sampled every 5 s but processed and archived as 1-hour averages. Data from April to September 1986 and July 1987 are used here, which include 54 pairs of clear-sky matched measurements made at different local times throughout the day. The pyranometers mounted on the Saskatoon tower are 10 m above the ground, and the data are recorded as 1-min mean values. To increase the aerial representation of the measurements made at Saskatoon, only winter data from December 1989 to February 1990 were used when the surface is uniformly covered by snow.

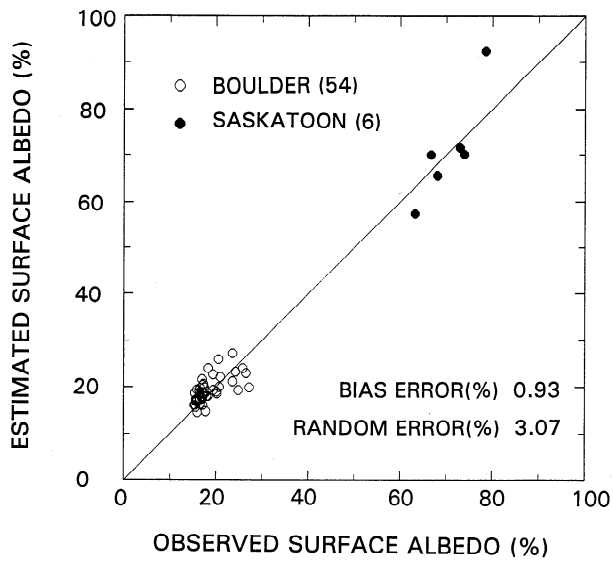

Figure 13. A comparison of the surface albedo estimated using the TOA albedos from ERBS and the simultaneous measurements from pyranometers mounted at two observation towers.

Six pairs of data are identified as being clear according to local weather reports. Precipitable water amounts are obtained from radiosonde measurements made at the closest meteorological stations.

Figure 13 compares the surface albedos observed at the two towers and estimated from the ERBS satellite. Note that the estimated albedos agree well with the measured ones at both locations representing very different surface types and atmospheric conditions. The bias and random errors are 1% and 3%, respectively. Bias error is defined as the mean difference between the estimated and observed albedo, and the random error is equal to the root-mean-square of the differences from which bias error is subtracted. It should be emphasized that the parameterization defined by (1)–(7) was used without any adjustment to the surface observations. The accuracy of the comparison confirms the robustness and accuracy of the parameterization. The moderate random error may be partly due to physical reasons, but it is, to a nonnegligible extent, associated with matching errors [*Li et al.*, 1993b]. As discussed above, the effective viewing areas of the pyranometers on the towers could be somewhat smaller than the FOV of the ERBE radiometer, owing to the effect of incident angle. Since the towers may be situated in any portion or even outside of a satellite FOV [*Cess et al.*, 1991], the matching error should be random. The random error due to imperfect matching should not be interpreted as the uncertainty of the algorithm. In any case, random errors will be reduced significantly by averaging. Considering the fact that substantial averaging is conducted in the process of obtaining the monthly mean data, it is reasonable to expect that the error in the estimate of the monthly mean albedo will be considerably smaller.

5. Climatology of Surface Broadband Albedo

5.1. Data

To generate a global climatology of surface albedo requires global data sets of clear-sky TOA albedo and precipitable water. The other input to the parameterization, the SZA, is known. The clear-sky albedo can be obtained globally from the ERBE data set. ERBE's scene identification algorithm assigns each pixel measurement as being clear, partly cloudy, mostly cloudy, and overcast. Preliminary assessment of the performance of the ERBE scene identification algorithm was conducted by *Diekmann and Smith* [1989] in low latitudes and *Li and Leighton* [1991] in high latitudes. Except for snow/ice surfaces, clear scenes identified by the ERBE are generally true, although it is not uncommon for a clear pixel to be misidentified as cloudy, or for a cloudy pixel to be assigned to an incorrect classification of cloudiness. However, clear scenes identified by ERBE over snow/ice are often questionable [*Li and Leighton*, 1991].

There are nominally 5 years of ERBE observations for which data are available ranging from 1985 to 1989, while the longest period of observation is from November 1984 to February 1990 made by ERBS. The data employed here are not the pixel data but one of the monthly mean products, namely the "regional, zonal, and global average product" designated as S-4, due to the limited occurrence of clear skies. The spatial resolution of this data is 2.5° × 2.5° latitude-longitude. The uncertainty for monthly mean shortwave data is estimated to be of the order of 5 Wm^{-2} due to calibration, sampling, and angular corrections etc. [*Barkstrom et al.*, 1989], which is equivalent to 1.5% in terms of daily mean TOA albedo for incident flux equal to solar constant (1365 Wm^{-2}). The clear data were obtained by averaging all the clear measurements falling within an area of 2.5° × 2.5° in a month. Daily mean values are derived from individual ones after correction for the diurnal variation using the ERBE angular dependence models.

Precipitable water amounts at the same resolution were derived from the model analyses produced at the ECMWF. The data include, among other parameters, temperature, relative humidity and geopotential height at seven pressure levels ranging from 1000 to 100 mbar. The humidity data are obtained by making use of radiosonde observations, satellite retrievals and a trial field consisting of a short-term forecast. The analyses are available twice daily at 0000 and 1200 GMT. Precipitable water is determined at each analysis time by integrating the water vapor mixing ratio from the surface to the top of the atmosphere using trapezoidal method. Daily and monthly means of precipitable water are obtained by averaging. Detailed discussions on the computation and global distributions of precipitable water amount from ECMWF data are given by *Li and Leighton* [1993]. The monthly mean precipitable water is employed together with the monthly mean clear-sky TOA albedo to generate a global climatology of surface broadband albedo. Since monthly mean precipitable water is obtained from the daily means for all days of a month, clear-sky precipitable water may be overestimated. To gain an insight into the resulting uncertainty in the estimates of surface albedo, we have collocated satellite-based cloud data and radiosonde humidity data for both winter and summer seasons over the regions of 20°S to 20°N and 50°N to 60°N. Over 1000 cases were processed, and the values of $\delta p/\sqrt{p}$ range from 0.2 in the tropics to 0.5 at high latitudes, as inferred from differences in mean p between satellite-identified clear scenes and the average of all data for a given latitude and season. Thus the uncertainty $\delta p/\sqrt{p}$ is smaller than that resulting from using the monthly mean climatology of precipitable water (0.7). From these

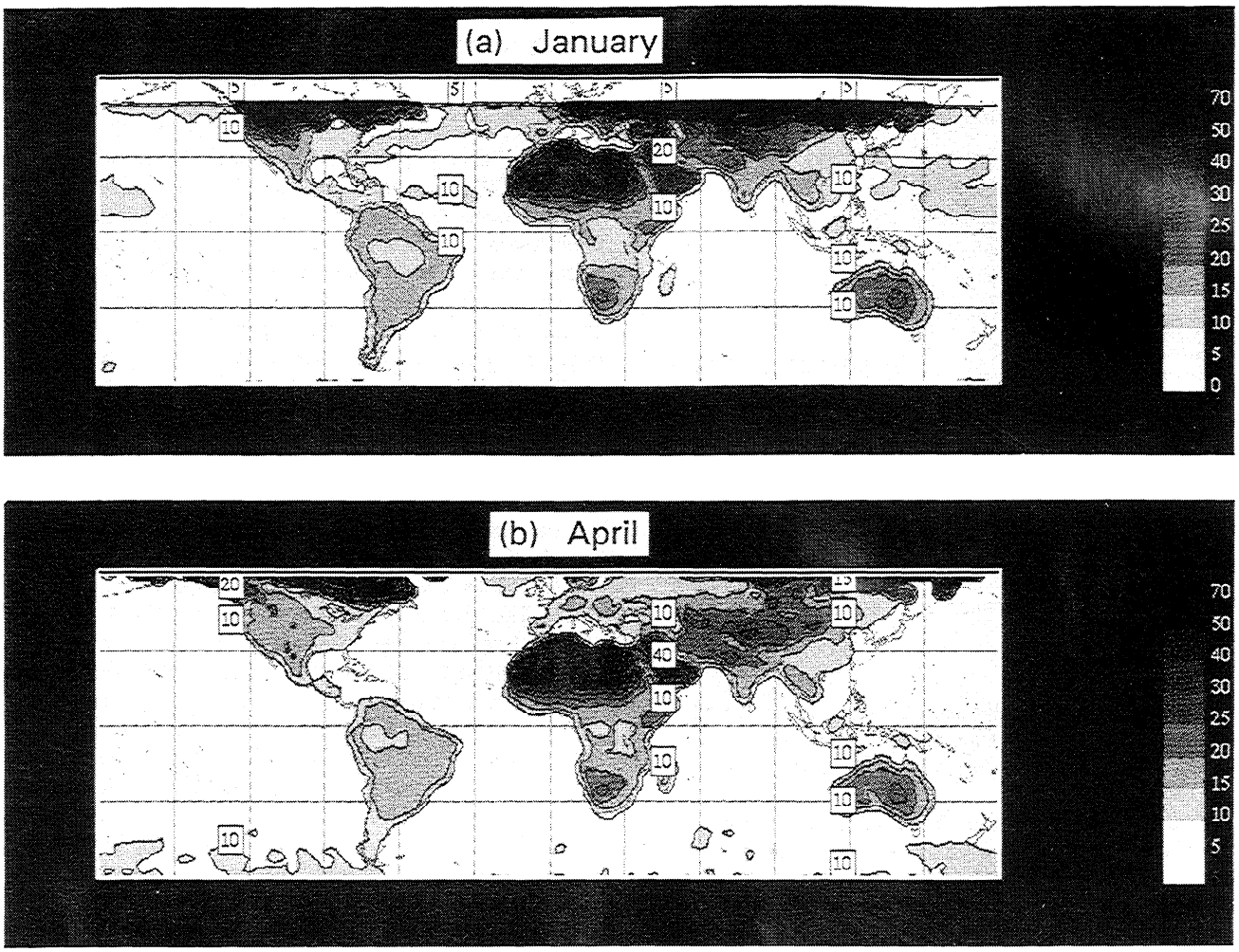

Figure 14. The geographical distribution of clear-sky surface broadband albedo for (a) January, (b) April, (c) July, and (d) October, derived from 5 years of ERBE data.

values and (13), the resulting uncertainty is estimated to be less than 1%.

5.2. Regional Variation of the Surface Albedo

Figure 14 presents the distribution of surface albedo for 4 months, representing each season from near 60°S to near 60°N. Similar maps were derived for the other months. High latitudes were excluded because of unreliable ERBE scene identification (unable to discriminate cloud from snow or ice) and because radiative transfer computations are subject to large errors at low sun angles. The μ cutoff was set to 0.2. The patterns of the geographical distribution of surface albedo are marked by minima over the tropical oceans and maxima over deserts and snow/ice surfaces. The snow/ice surfaces have albedos typically in the range of 55 to 80%. The surface albedo over land generally ranges from 10 to 30% depending on factors such as vegetation type, coverage, and soil moisture. The surface albedo over deserts varies from one desert to another. The brightest desert is the Sahara with values ranging from 35 to 49%, in good agreement with *Barker and Davies* [1989]. *Rockwood and Cox* [1978] reported airborne measurements of surface albedo over Northwestern Sahara with a mean of 43% and a standard deviation of 2.1%. Current estimates over the same region range from 40 to 45%. The surface albedo of the Saudi desert ranges from 35 to 43%. Albedos for other major deserts such as Gibson (Australia), Gobi (China) or Kalahari (Botswana) are generally less than 30%. The magnitude and spatial variation pattern over Africa match well with the results of *Arino et al.* [1991]. The current estimates of surface albedos of the major deserts are significantly higher than those used by many GCMs whose values were given by *Barker and Davies* [1989]. As expected, the snow/ice boundary stands out clearly on the maps, as surface albedo increases dramatically from snow/ice-free regions to snow/ice-covered regions. The surface albedo of snow/ice inside the snow/ice boundary also varies greatly associated with the status of snow/ice. Because of the striking variation of surface albedo over land as opposed to that over oceans, the variability of the oceanic albedo does not appear in the plots. In fact, the oceanic surface albedo ranges from 6% to more than 10% in the domain shown here, mainly due to the effect of SZA (as expected from Figure 2). Low albedos of around 6% can be found over tropical oceans or subtropical oceans during their summer seasons. The estimated surface albedos are compared in detail with those used in the Canadian Climate Centre's general circulation model [*Barker et al.*, 1994]. In addition to the major deserts, moderate differences were found over oceans of the winter hemispheres, land of many small lakes, and snow/ice surfaces. Most of the

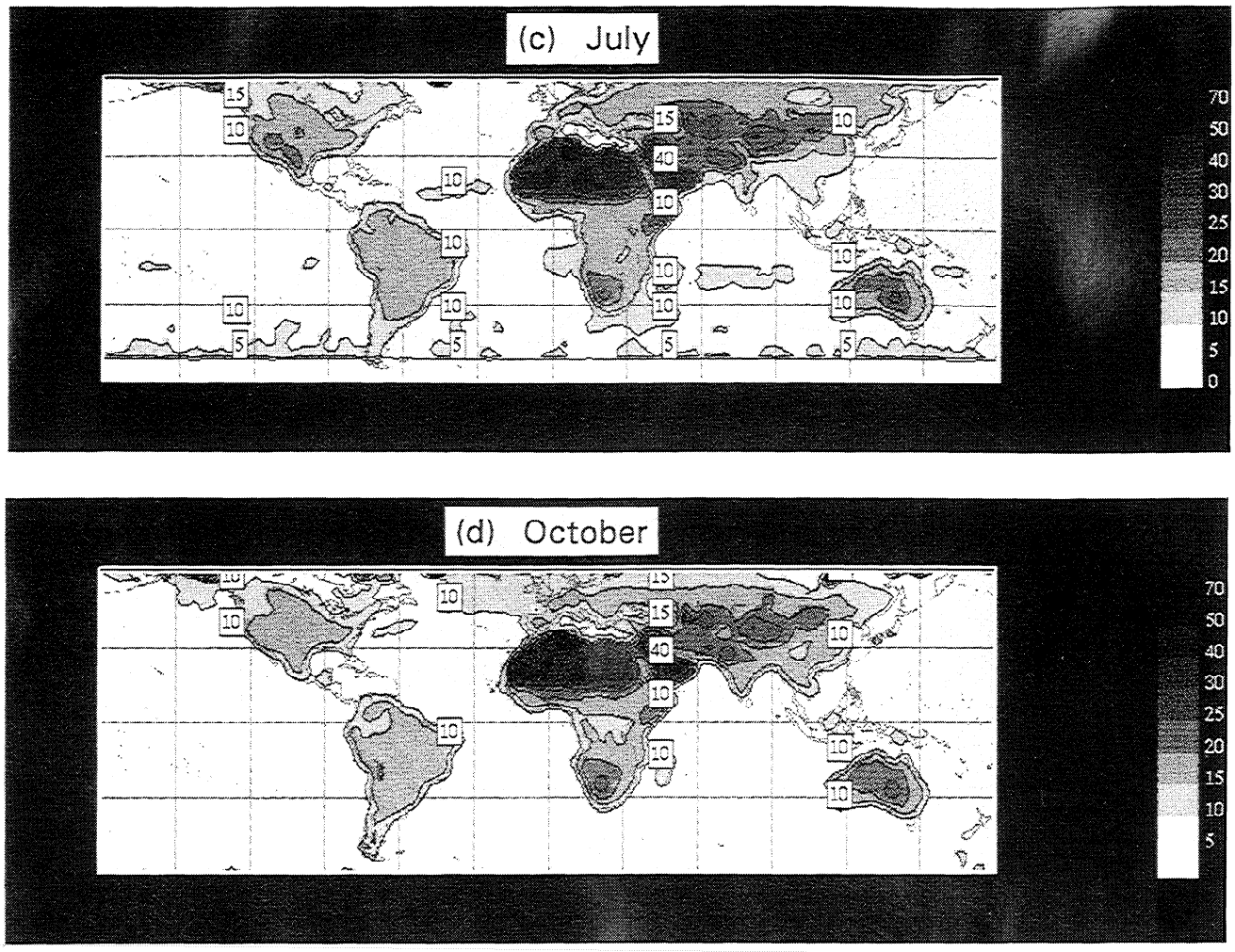

Figure 14. (continued)

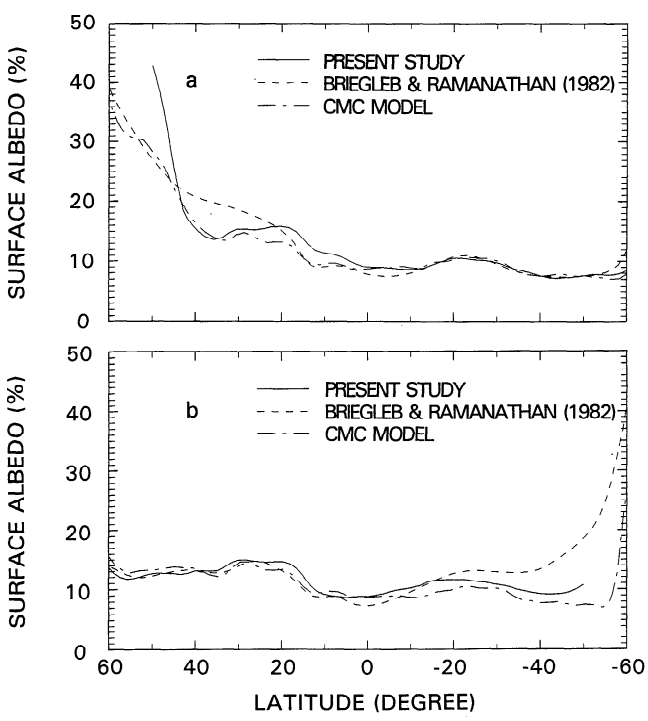

Figure 15. Latitudinal variations of zonal mean surface albedos for (a) January and (b) July derived from the present study, the study by *Briegleb and Ramanathan* [1982], and the CMC database.

differences have been attributed to the deficiencies in the GCM albedo data.

5.3. Zonal Mean Variation of Surface Albedo

Figure 15 presents the zonal mean surface albedos derived from regional values, and are compared to those of *Briegleb and Ramanathan* [1982] (hereafter referred to as BR), and those used by the Canadian Meteorological Centre's (CMC) numerical prediction model, which were originally derived from *Wilson and Henderson-Sellers* [1985]. It follows from Figure 15a that in January this study's albedos agree with those of CMC within 1% for most latitudes except between 0° and 25° and north of 42°. The discrepancies in these two regions can be attributed to the systematic lower albedos used for desert and snow/ice surfaces by the CMC model. For example, surface albedos of snow and ice used by the CMC are only 55% and 45%, respectively. In July the comparison is generally better than in January (Figure 15b). Overall, the differences between the results of this study and the BR study are greater than those used in CMC. It should be pointed out that BR computed the TOA albedo from their compiled surface albedo. The satellite-measured TOA albedo is thus useful to test their surface albedo. The comparison of the TOA albedo bears a close resemblance to that of the surface albedo. This is a good indication that the present study's results are likely to be of superior quality, inasmuch

(a) January

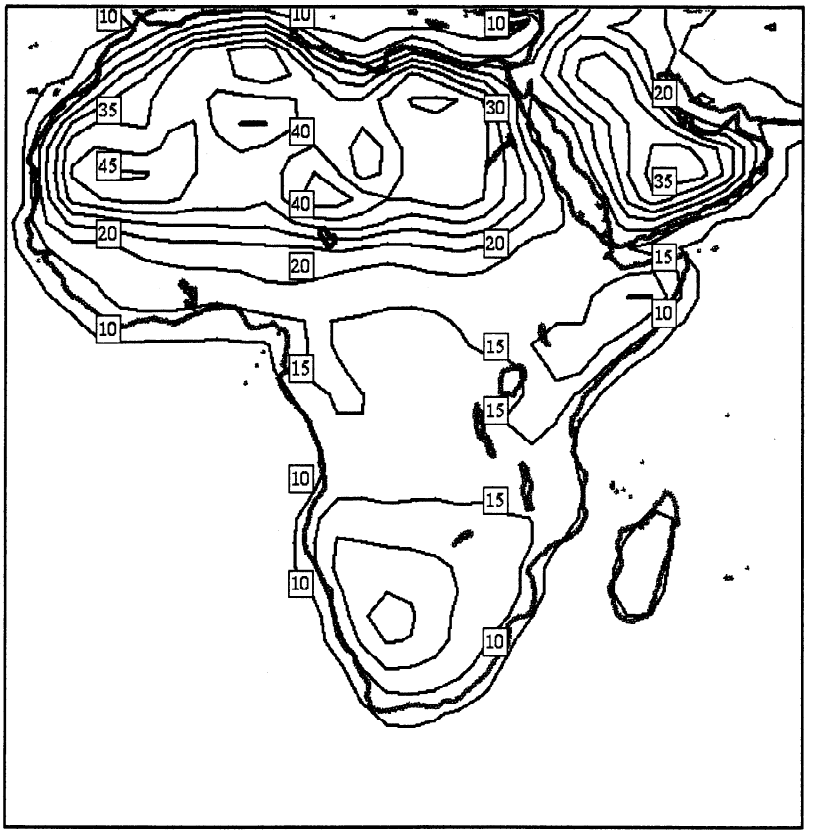

(b) July

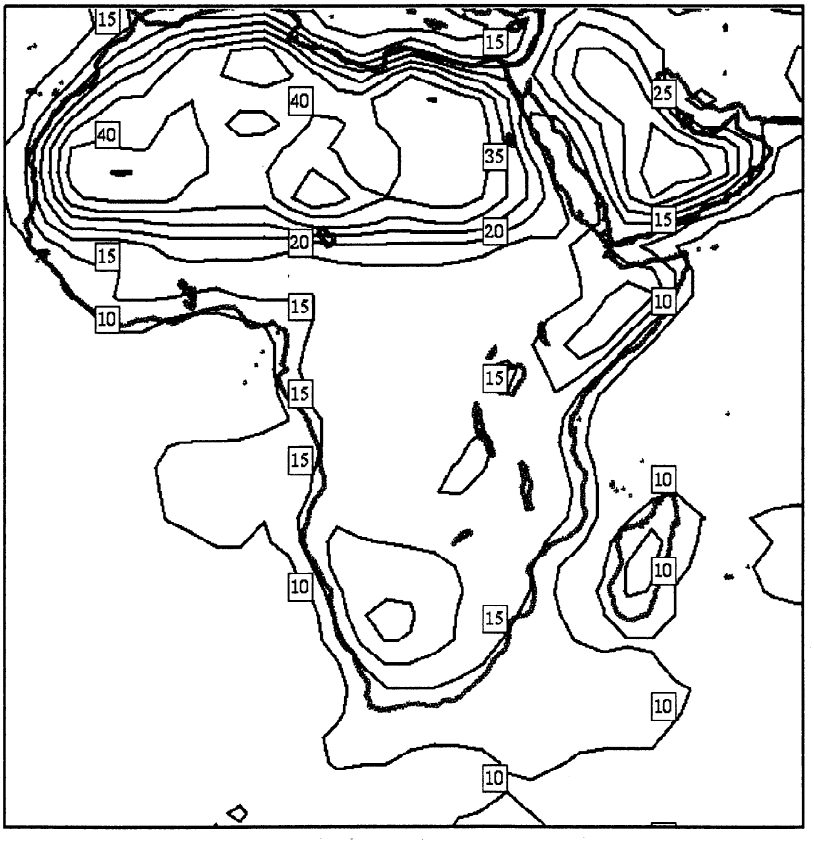

Figure 16. Monthly mean albedo (5% intervals) over a region centered on the African continent for (a) January, (b) July, and (c) the difference (July minus January) with a contour interval of 2%. Specific sites A–F referred to in the text and in Table 1 are also shown.

(c) July - January

Figure 16. (continued)

as the TOA albedo observed by ERBE is more reliable than the calculated TOA albedo by BR. As a result of this study, the CMC surface albedo climatology is being modified, especially over deserts and snow/ice-covered regions. Over oceans a constant surface albedo of 7% was used until now.

Table 1. Monthly Mean Surface Albedo (%) at Selective Points (2.5° × 2.5° Areas) Indicated in Figure 16c

	A	B	C	D	E	F
Jan.	21.7	20.0	20.0	43.3	17.8	6.9
Feb.	23.1	20.5	20.7	43.3	17.3	6.7
March	23.1	20.2	21.5	41.8	19.0	7.5
April	24.3	21.4	22.0	41.3	18.7	8.7
May	23.6	19.6	21.0	42.9	18.3	10.9
June	22.1	19.1	25.9	44.1	18.1	11.2
July	17.2	16.7	25.7	43.7	18.2	11.1
Aug.	18.3	17.0	25.2	43.6	19.4	9.9
Sept.	19.1	17.4	22.9	43.5	19.1	11.1
Oct.	21.1	19.3	22.8	43.1	19.7	8.3
Nov.	20.9	19.7	21.8	43.1	18.8	7.9
Dec.	20.7	19.4	20.9	43.4	18.0	7.0

Key: A, Nigeria (10.0°N, 12.5°E); B; Sudan (10.0°N, 30.0°E); C, Somalia (2.5°N, 42.5°E); D, Saudi Arabia (20.0°N, 50.0°E); E, Zimbabwe-Zambia border (17.5°S, 27.5°E); and F, ocean (12.5°S, 2.5°E).

Again, this study's results will correct this unrealistic simplification.

5.4. Seasonal Variation of Surface Albedo

Except over deserts, surface albedo is subject to significant annual variation in conjunction with the changes of SZA, vegetation, precipitation, snowfall, etc. A detailed study of these variations is beyond the scope of this paper. However, a broad region, where snow or ice is almost totally absent, is examined here more closely. Figure 16 represents an enlargement of Figure 14 for the African continent and Saudi Arabia in January (Figure 16a) and July (Figure 16b). The maximum contours of 35% and 40% over the Sahara and Saudi deserts are very similar for the two seasons and point by point differences are generally less than 1%. The same remarks apply to the 20% and 25% contours of the Kalahari desert. These results are indicative of the robustness of the technique, considering the fact that the difference in sun angle amounts to 50° between the 2 months over the same region. Figure 16c shows the difference between the albedos of July and January. Maximum differences are about 6%.

Six specific points, A to F, were selected in regions of interest. Points A, B, C, and F are sectors where maximum seasonal differences were retrieved. Point D should be a fairly stable target, since it represents the region of maximum albedo in the Saudi desert. Point E is a mountainous region characterized by a moderate albedo. For each of these points, the 12 monthly means are listed in Table 1.

Points A and B are characterized by a maximum albedo in April, with a sharp decrease between June and July. This trends appears to be real since albedos remain low in August and slowly increase afterward. The rapid change in albedo in July is likely due to the progress across 10°N of the intertropical convergence zone resulting in more precipitation at point A and B in the range 200–400 mm [*Global Precipitation Climatology Centre* (*GPCC*), 1992]. In July, precipitations in excess of 50 mm per month occur almost exclusively north of the equator in Africa. This explains a good part of the negative differences of 1–4% in Figure 16c in the latitude belt 0°–20°N. The trend at point C is of opposite sign with maximum albedos of about 25% in the summer months, most likely due to the dryness of the soil. This part of Somalia receives most of its rain in the spring and fall months; virtually no rain falls during the summer and winter months. In summer the surface dries quickly due to strong insolation. The Saudi desert, point D, has a very stable albedo with a typical value of 43.3%. Lower values near 41.5% in March and April may be explained by the fact that monthly precipitation in the range of 10 to 25 mm only occurs in those months [*GPCC*, 1992]. Albedos at target E vary only by about 2%, with no clearly defined seasonal trends, except for the lowest albedos observed once again during the rainy season (December–February). Finally, point F is an oceanic point at a latitude where it is normal to expect an increase in albedo from about 7% in January to 9.5% in July because of the increase in solar zenith angle (see Figure 2). The albedos of 11% are certainly too high by about 1.5%. Since the overestimates occur at times when the daily mean Sun angle is low (winter months), the error is likely due to the uncertainty associated with the bidirectional reflectance model. In particular, sunglint effects may easily cause such errors. Residual cloud contamination could be another cause of the ocean albedo being too high. The same analysis applies to other low-latitude oceanic regions in Figure 14, where the albedo exceeds 10%. For example, broad regions with ocean albedo greater than 10.0% are noted in Figure 14a (January), but maximum albedos do not exceed 11.0%.

Examination of data such as those of Table 1 indicates that, superimposed on the detected seasonal trends, there exists a random error component of less than 1% in terms of absolute albedo. The method appears capable of detecting seasonal variations of more than 1% in surface albedo, since the typical absolute difference in individual monthly mean albedo estimates is consistent from month to month to within a fraction of 1%. This level of signal detectability is satisfactory, and an absolute error estimate of 1% on monthly 2.5° × 2.5° areas appears realistic provided that the ERBE calibration and bidirectional models introduce no significant bias.

6. Summary

Surface albedo is one of the important but poorly observed climatic parameters. Because of the limitations inherent to the surface observations, there have been many attempts to retrieve surface albedo from satellite measurements. Most of them, however, suffer from one or more limitations. They include the simplification of radiative transfer models applied to ideal surface and atmospheric conditions, the use of imperfect narrowband measurements converted to broadband values, the lack of angular correction, and inflight calibration.

In this study, a double-adding radiative transfer model was applied to a vertically inhomogeneous atmosphere over various surface types. Scattering and absorption by atmospheric molecules and aerosol were taken into account. Different surface types were characterized by different spectral and angular dependencies of albedo. The results of the computations confirm that the commonly used simple linear relationship is a powerful tool in deriving surface albedo from satellite-measured TOA albedo. The linear relationship still retains an acceptable accuracy when both angular and spectral effects are incorporated. The relationship is controlled strongly by solar zenith angle and precipitable water. A simple parameterization was thus derived with three input parameters: TOA albedo, solar zenith angle, and precipitable water. The technique was proven to be applicable for the estimation of both instantaneous and daily mean surface albedos. Sensitivity tests of the parameterization were done to the temperature profile, precipitable water, aerosol, carbon dioxide, and ozone. All of the parameters except precipitable water and aerosol have negligible effects on the relationship between TOA and surface albedos. The magnitude of the aerosol effect depends on surface albedo. It is large for low and high albedos and small for moderately high albedos. Preliminary validation using collocated observations from satellites and observation towers shows a bias error of 1% and a random error of 3%. Considering that the random error is, to some extent, due to imperfect collocation, the real accuracy of the retrieval may be well suitable for climate studies. A global climatology of clear-sky surface broadband albedo was then developed by applying the parameterization to the 5-year ERBE and ECMWF data sets. Regional, zonal, and temporal variations of the derived albedo were analyzed and compared with those obtained from other sources. In general, the results compare favorably with other satellite-based estimates, whereas large systematic differences were noted for certain types of surfaces such as deserts and snow/ice when compared with the values used in some GCM and NWP models. Analyses of seasonal variations of surface albedo reveal that the parameterization has 1% (absolute value) signal detectability.

In summary, the proposed parameterization appears to be a valid candidate for routine application on a global scale; it combines the advantages of simplicity, robustness and reasonable accuracy. We did not quantify the uncertainties resulting from erroneous identification of clear scenes and uncertainties in angular dependence models. Previous work indicated that these factors may lead to significant errors in the estimates of surface albedo from satellite observations. As satellite observation techniques ameliorate, the uncertainties associated with these factors will diminish significantly, especially in the era of the Earth Observation System (EOS) that will commence near the end of the century.

Acknowledgments. The criticisms of the anonymous reviewers were very useful in improving the clarity and the quality of the manuscript. We would like to thank K. Masuda and T. Takashima for providing the results of radiative transfer simulations and their model. Tower observations were kindly provided by R. Cess and L. J. B. McArthur. Comments from H. Barker and G. Deblonde are gratefully acknowledged. This work was supported partially by the Natural Sciences and Engineering Research Council (NSERC) of Canada while ZL was a visiting fellow at the Atmospheric Environment Service of Canada.

References

Arino, O., G. Dedieu, and P. Y. Deschamps, Accuracy of satellite land surface reflectance determination, *J. Appl. Meteorol.*, *30*, 960–972, 1991.

Barker, H., and J. Davies, Surface albedo estimates from Nimbus-7 ERB data and a two-stream approximation of the radiative transfer equation, *J. Clim.*, *2*, 409–418, 1989.

Barker, H. W., Z. Li, and J.-P. Blanchet, Radiative characteristics of the Canadian Climate Centre second-generation general circulation model, *J. Clim.*, in press, 1994.

Barkstrom, B. R., and G. L. Smith, The Earth radiation budget experiment: Science and implementation, *Rev. Geophys.*, *24*, 379–390, 1986.

Barkstrom, B., E. Harrison, G. Smith, R. Green, J. Kibler, R. Cess, and the ERBE Science Team, Earth radiation budget experiment (ERBE) archival and April 1985 results, *Bull. Am. Meteorol. Soc.*, *70*, 1254–1262, 1989.

Blanchet, J.-P., and R. List, Estimation of optical properties of Arctic haze using a numerical model, *Atmos. Ocean*, *21*, 444–465, 1983.

Bowker, D. E., R. E. Davis, D. L. Myrick, K. Stacy, and W. T. Jones, Spectral reflectance of natural targets for use in remote sensing studies, *NASA Ref. Publ.*, *1139*, 181 pp., 1985.

Brest, C. L., and S. N. Goward, Deriving surface albedo measurements from narrow band satellite data, *Int. J. Remote Sens.*, *8*, 351–367, 1987.

Briegleb, B., and V. Ramanathan, Spectral and diurnal variations in clear sky planetary albedo, *J. Appl. Meteorol.*, *21*, 1160–1171, 1982.

Briegleb, B., P. Minnis, V. Ramanathan, and E. Harrison, Comparison of regional clear-sky albedo inferred from satellite observations and model computations, *J. Clim. Appl. Meteorol.*, *25*, 214–226, 1986.

Cess, R. D., Biosphere-albedo feedback and climate modelling, *J. Atmos. Sci.*, *35*, 1765–1768, 1978.

Cess, R. D., and I. L. Vulis, Inferring surface solar absorption from broadband satellite measurements, *J. Clim.*, *2*, 974–985, 1989.

Cess, R. D., E. G. Dutton, J. J. DeLuisi, and F. Jiang, Determining surface solar absorption from broadband satellite measurements for clear skies: Comparisons with surface measurements, *J. Clim.*, *4*, 236–247, 1991.

Cess, R. D., S. Nemesure, E. G. Dutton, J. J. DeLuisi, G. L. Potter, and J.-J. Morcrette, The impact of clouds on the shortwave radiation budget of the surface-atmosphere system: Interfacing measurements and models, *J. Clim.*, *6*, 308–316, 1993.

Charney, J. G., W. J. Quirk, S. M. Chew, and J. Kornfield, A comparative study of the effects of albedo change on drought in semi-arid regions, *J. Atmos. Sci.*, *34*, 1366–1388, 1977.

Chen, T. S., and G. Ohring, On the relationship between clear-sky planetary and surface albedos, *J. Atmos. Sci.*, *41*, 156–158, 1984.

Choudhury, B. J., Multispectral satellite data in the context of land surface heat balance, *Rev. Geophys.*, *29*, 217–236, 1991.

Cox, C., and W. Munk, Slopes of the sea surface deduced from photographs of the Sun glitter, *Bull. Scripps Inst. Ocean.*, *6*, 401–488, 1956.

Dickinson, R. E., Land surface processes and climate-surface albedos and energy, *Adv. Geophys.*, *25*, 305–353, 1983.

Dickinson, R. E., P. J. Sellers, and D. S. Kimes, Albedos of homogeneous semi-infinite canopies: Comparison of two-stream analytic and numerical solutions, *J. Geophys. Res.*, *92*, 4282–4286, 1987.

Dickinson, R. E., B. Pinty, and M. M. Verstraette, Relating surface albedos in GCMs to remotely sensed data, *Agric. For. Meteorol.*, *52*, 109–131, 1990.

Diekmann, F. J., and G. L. Smith, Investigation of scene identification algorithms for radiation budget measurements, *J. Geophys. Res.*, *94*, 3395–3412, 1989.

Global Precipitation Climatology Centre, *Monthly Precipitation Estimates Based on Gauge Measurements on Continents for the Year 1987 (Preliminary Results) and Future Requirements*, (ISBN 3-88148-276-8), 20 pp., Global Precipitation Climatology Centre, Offenbach am Main, Germany.

Gutman, G., A simple method for estimating monthly mean albedo of land surfaces from AVHRR data, *J. Appl. Meteorol.*, *27*, 973–988, 1988.

Gutman, G., G. Ohring, D. Tarpley, R. Ambroziak, Albedo of the U.S. great plains as determined from NOAA-9 AVHRR data, *J. Clim.*, *2*, 608–617, 1989a.

Gutman, G., A. Gruber, D. Tarpley, and R. Taylor, Application of angular models to AVHRR data for determination of the clear-sky planetary albedo over land surfaces, *J. Geophys. Res.*, *94*, 9959–9970, 1989b.

Henderson-Sellers, A., and M. F. Wilson, Surface albedo data for climatic modelling, *Rev. Geophys.*, *21*, 1743–1778, 1983.

Iqbal, M., *An Introduction to Solar Radiation*, 390 pp., Academic, San Diego, Calif., 1983.

Kimes, D. S., Dynamics of directional reflectance factor distributions for vegetation canopies, *Appl. Opt.*, *22*, 1364–1372, 1983.

Kimes, D. S., Modelling the directional reflectance from complete homogeneous vegetation canopies with various leaf orientation distribution, *J. Opt. Soc. Am.*, *1*, 725–737, 1984.

Kimes, D. S., P. J. Sellers, and D. J. Diner, Extraction of spectral hemispherical reflectance (albedo) of surfaces from nadir and directional reflectance data, *Int. J. Remote Sens.*, *8*, 1727–1746, 1987.

Kneizys, F. X., E. P. Shettle, W. O. Gallery, J. H. Chetwynd, Jr., L. W. Abreu, J. E. A. Selby, S. A. Chough, and R. W. Fenn, Atmospheric transmittance/radiance: Computer code LOWTRAN 6, *Rep. AFGL-TR-83-0187*, 200 pp., Air Force Geophysics Laboratory, Bedford, Mass., 1983.

Koepke, P., and K. T. Kriebel, Improvements in the shortwave cloud-free radiation budget accuracy, Part I, Numerical study including surface anisotropy, *J. Clim. Appl. Meteorol.*, *26*, 374–395, 1987.

Kriebel, K. T., Measured spectral bidirectional reflection properties of four vegetated surfaces, *Appl. Optics*, *17*, 253–259, 1978.

Kukla, G., and D. Robinson, Annual cycle of surface albedo, *Mon. Weather Rev.*, *108*, 56–68, 1980.

Li, Z., and H. G. Leighton, Scene identification and its effect on cloud radiative forcing in the Arctic, *J. Geophys. Res.*, *96*, 9175–9188, 1991.

Li, Z., and H. G. Leighton, Narrowband to broadband conversion with spatially autocorrelated reflectance measurements, *J. Appl. Meteorol.*, *31*, 421–432, 1992.

Li, Z., and H. G. Leighton, Global climatology of solar radiation budgets at the surface and in the atmosphere from 5 years of ERBE data, *J. Geophys. Res.*, *98*, 4919–4930, 1993.

Li, Z., H. G. Leighton, K. Masuda, and T. Takashima, Estimation of SW flux absorbed at the surface from TOA reflected flux, *J. Clim.*, *6*, 317–330, 1993a.

Li, Z., H. G. Leighton, and R. D. Cess, Surface net solar radiation estimated from satellite measurements: Comparisons with tower observations, *J. Clim.*, *6*, 1764–1772, 1993b.

Lian, M. S., and R. D. Cess, Energy balance climate models: A reappraisal of ice-albedo feedback, *J. Atmos. Sci.*, *34*, 1058–1062, 1977.

Liu, W. T., W. Tang, and F. J. Wentz, Precipitable water and surface humidity over global oceans from special sensor microwave image and European Center for Medium-range Weather Forecasts, *J. Geophys. Res.*, *97*, 2251–2264, 1992.

Masuda, K., and T. Takashima, Computational accuracy of radiation emerging from the ocean surface in the model atmosphere-ocean system, *Pap. Met. Geophys.*, *37*, 1–13, 1986.

Masuda, K., and T. Takashima, Sensitivity of radiation absorbed in the ocean to atmospheric and oceanic parameters in the short wavelength region, Part 1, Cloudless atmosphere, *J. Meteorol. Soc. Jpn.*, *66*, 617–628, 1988.

Matthews, E., and W. B. Rossow, Regional and seasonal variations of surface reflectance from satellite observations at 0.6 μm, *J. Clim. Appl. Meteorol.*, *26*, 170–202, 1987.

McClatchey, R. A., R. W. Fenn, J. E. A. Selby, F. E. Volz, and J. S. Garing, Optical properties of the atmosphere, *Rep. AFCRL-71-0279*, 85 pp., 1971. (Available from Air Force Cambridge Res. Lab., Cambridge, Mass.)

Nemesure, S., R. D. Cess, E. G. Dutton, J. J. DeLuisi, Z. Li, and H. G. Leighton, Impact of clouds on the shortwave radiation budget of the surface-atmosphere system for snow-covered surfaces, *J. Clim.*, in press, 1994.

Nunez, M., W. J. Skirving, and N. R. Viney, A technique for estimating regional surface albedos using geostationary satellite data, *J. Climatol.*, *7*, 1–11, 1987.

Ohmura, A., and H. Gilgen, Reevaluation of the global energy

balance, in *Interactions Between Global Climate Subsystems: The Legacy of Hann, Geophys. Monogr. Ser.*, vol. 75, edited by G. A. McBean and M. Hantel, pp. 93–110, AGU, Washington, D. C., 1993.

Paltridge, G., and C. Platt, *Radiative Processes in Meteorology and Climatology*, 318 pp., Elsevier, New York, 1976.

Pinker, R. T., Determination of surface albedo from satellite, *Adv. Space Res.*, *5*, 333–343, 1985.

Pinker, R. T., and L. L. Stowe, Modelling planetary bidirectional reflectance over land, *Int. J. Remote Sens.*, *11*, 113–123, 1990.

Pinty, B., and D. Ramond, A method for the estimate of broadband surface albedo from a geostationary satellite, *J. Clim. Appl. Meteorol.*, *26*, 1709–1722, 1987.

Pinty, B., and G. Szejwach, A new technique for inferring surface albedo from satellite observations, *J. Clim. Appl. Meteorol.*, *24*, 741–750, 1985.

Pinty, B., and M. M. Verstraete, On the design and validation of surface bidirectional reflectance and albedo models, *Remote Sens. Environ.*, *41*, 155–167, 1992.

Pinty, B., M. M. Verstraete, and R. E. Dickinson, A physical model of the bidirectional reflectance of vegetation canopies, Part 2, Inversion and validation, *J. Geophys. Res.*, *95*, 11,767–11,775, 1990.

Posey, J. W., and P. F. Clapp, Global distribution of normal surface albedo, *Geofis Int.*, *4*, 33–48, 1964.

Potter, G. L., H. W. Elsasser, M. C. MacCracken, and J. S. Ellis, Albedo change by man: Test of climatic effects, *Nature*, *291*, 47–50, 1981.

Preuss, H. J., and J. F. Geleyn, Surface albedos derived from satellite data and their impact on forecast models, *Arch. Meteorol. Geophys. Bioklimatol., Ser. A*, *29*, 345–356, 1980.

Robock, A., The seasonal cycle of snow cover, sea ice, and surface albedo, *Mon. Weather Rev.*, *108*, 267–285, 1980.

Rockwood, A. A., and S. K. Cox, Satellite-infrared surface albedo over Northwestern Africa, *J. Atmos. Sci.*, *35*, 513–522, 1978.

Sellers, P. J., Canopy reflectance, photosynthesis and transpiration, *Int. J. Remote Sens.*, *6*, 1335–1372, 1985.

Sellers, P. J., S. I. Rasool, and H.-J. Bolle, A review of satellite data algorithms for studies of the land surface, *Bull. Am. Meteorol. Soc.*, *71*, 1429–1447, 1990.

Shaw, G., Atmospheric turbidity in the polar regions, *J. Appl. Meteorol.*, *21*, 1080–1088, 1982.

Suttles, J. T., R. N. Green, P. Minnis, G. L. Smith, W. F. Staylor, B. A. Wielicki, I. J. Walker, D. F. Young, V. R. Taylor, and L. L. Stowe, Angular radiation models for Earth-atmosphere system, vol. 1, Shortwave radiation, *NASA Ref. Publ.*, *1184*, 114 pp., 1988.

Tsay, S. C., K. Stamnes, and K. Jayaweera, Radiative energy budget in the cloudy and hazy Arctic, *J. Atmos. Sci.*, *46*, 1002–1018, 1989.

Verstraete, M. M., Radiation transfer inplant canopies: scattering of solar radiation and canopy reflectance, *J. Geophys. Res.*, *93*, 9483–9494, 1988.

Verstraete, M. M., B. Pinty, and R. E. Dickinson, A physical model of the bidirectional reflectance of vegetation canopies, Part 1, Theory, *J. Geophys. Res.*, *95*, 11,755–11,765, 1990.

Warren, S. G., and W. J. Wiscombe, A model for the spectral albedo of snow, II, Snow containing atmospheric aerosols, *J. Atmos. Sci.*, *37*, 2734–2745, 1980.

Whitlock, C. H., G. C. Purgold, and S. R. LeCroy, Surface bidirectional reflectance properties of two southwestern Arizona deserts for wavelengths between 0.4 and 2.2 micrometers, *NASA Tech. Pap.*, *2643*, 44 pp., 1987. (Available from NASA, Code NTT-4, Washington, D. C., 20546-0001.)

Wilson, M. F., and A. Henderson-Sellers, A global archive of land cover and soils data for use in general circulation climate models, *J. Clim.*, *5*, 119–143, 1985.

Wiscombe, W. J., and S. G. Warren, A model for the spectral albedo of snow, I, Pure snow, *J. Atmos. Sci.*, *37*, 2712–2733, 1980.

L. Garand, Atmospheric Environment Service, 2121 Trans-Canada Highway, Dorval, Quebec, Canada H9P 1J3.

Z. Li, Canada Centre for Remote Sensing, 588 Booth St., Ottawa, Ontario, Canada K1A 0Y7.

(Received February 22, 1993; revised January 14, 1994; accepted January 20, 1994.)